Supplementary Materials

High-speed complex field modulation using binary phase-engraved superpixels

Patrick Kilcullen[1], Jingdan Liu[1,†], Youmin Wang[2], Lei Gong[3], Jinyang Liang[1,*]

[1]Laboratory of Applied Computational Imaging, Centre Énergie Matériaux Télécommunications, Institut National de la Recherche Scientifique, Université du Québec, 1650 boulevard Lionel-Boulet, Varennes, Québec J3X1P7, CANADA

[2]Reality Laboratory, Meta Platforms, 9845 Willows Road, Redmond, Washington 98052, USA

[3]Department of Optics and Optical Engineering, University of Science and Technology of China, 96 JinZhai Road, Hefei, Anhui 230026, CHINA

[†]Current address: Shanghai Institute of Optics and Fine Mechanics, Chinese Academy of Sciences, Shanghai 201800, CHINA

*Corresponding author: jinyang.liang@inrs.ca

Supplementary Note 1: Details and operation of the Texas Instruments phase light modulator

The phase light modulator (PLM) used in this work (Texas Instruments DLP6750Q1EVM) is, at present, distributed as a prototype evaluation module kit consisting of a controller board that interfaces with a computer and a satellite board on which the PLM chip is mounted. Two flexible ribbon cables interface the controller and satellite boards. The PLM chip (Fig. S1a) contains a physical array of 1358×800 ($W \times H$) micromirrors (10.8 μm pitch, 10.5 μm×10.5 μm in size) that are addressed by a 2716×1600 array of CMOS memory cells (Fig. S1b). The micromirrors are flexure-based monolithic structures that are actuated via the application of a fixed bias voltage to any of four electrodes fabricated beneath each micromirror (Fig. S1c). The displacement of each micromirror, generated via the electrodes, is digitally controlled by 4 bits of dedicated memory allocated as a block of 2×2 cells within the memory array (Figs. S1d and e). Finally, compatibility of the PLM with different light sources is supported via control of a bias voltage applied to the micromirror membranes themselves, thus allowing the range of possible micromirror displacements to be tuned to suit specific wavelengths.

During operation, data from the computer was transferred to the controller board through a DisplayPort interface configured to mirror the computer's graphical display at a resolution of 2716×1600 pixels, refreshed at 60 Hz with 24-bit color depth. Under this configuration, pixels

displayed by the computer were mapped directly to the memory cells of the PLM chip, with color information separated by the controller board into a set of bitplanes comprising 24 binary images that were sequentially displayed by the PLM at a fixed refresh rate of 1.44 kHz. This arrangement served as the basis by which control patterns, specified as binary data configuring the desired micromirror actuation states via the PLM's memory array, could be transferred to the PLM in aggregate for high-speed display in groups of up to 24 frames. Trigger signals provided by the controller board allowed the collection of CCD image data to be synchronized with the 1.44 kHz refresh rate of the PLM during experiments.

Supplementary Note 2: Details of system alignment

For superpixel modulation techniques, system performance depends strongly on the correct relative offset of the optical axes of lenses L1 and L2 (see Fig. 1b in Main Text), which creates the effective phase gradient across the surface of the used spatial light modulator (SLM). For the setup developed in this work, alignment was carried out using the following procedure. First, a standard 4-f imaging system was constructed, which imaged the PLM directly to the CCD sensor. The spatial filter was located at the Fourier plane and centered on the zeroth diffraction order seen from the PLM on the shared optical axis between lenses L1 and L2. Second, a binary phase grating corresponding to equation (2) in Main Text with $\tilde{T}(u,v) = 1$ and $R = R_{\mathrm{PLM}}$ was loaded onto the PLM, creating a series of diffraction orders seen at the Fourier plane. The lateral position of L1 was then adjusted so as to center the appropriate 1$^{\mathrm{st}}$ diffraction order on the spatial filter, with alignment guided via the optimization of the total power transmitted through the iris. Finally, with the binary grating pattern still displayed, the offset bias voltage of the PLM device was tuned to optimize the optical power transmitted through the spatial filter. The control of arbitrary complex fields via binary phase engraved (BiPE) superpixel-based complex light modulation (CFM) then took place without further modifications to the optical setup.

Supplementary Note 3: Theoretical comparison of diffraction efficiency between BiPE and binary amplitude-based superpixel complex field modulation

In comparison to binary amplitude-based superpixels, BiPE superpixels improve optical efficiency for CFM owing to the positioning of its spatial filter relative to the optical axis of lens L1 (see Fig. 1b in Main Text). For both methods, this position is determined by the phase gradient required

to supply the range of phase pre-factors available to the individual pixels on the deployed SLM within each superpixel. Whereas binary amplitude-based superpixels require this range to be $[0,2\pi]$ radians in order to support the creation of arbitrary complex fields, BiPE superpixels can use a reduced range of $[0,\pi]$ radians owing to their use of phase modulation. As a result, the phase gradient induced at the SLM surface, and thus the offset of the spatial filter relative to the zeroth diffraction order, is correspondingly halved for BiPE superpixels compared to binary amplitude-based superpixels. Expressions for the phase gradients and spatial filter positions of both methods are summarized in Table S1, and illustrated in Fig. S2.

To evaluate the optical efficiency advantage conferred by the spatial filter position in superpixel-based CFM, we modeled the scalar field $u(x,y)$ produced by an SLM as the convolution of a square micromirror $u_{\mathrm{p}}(x,y)$ with a function $a(x,y)$ representing a periodic array illuminated at an angle θ,

$$u(x,y) = u_{\mathrm{p}}(x,y) * a(x,y) \ , \tag{S1}$$

where

$$u_p(x,y) = \mathrm{rect}\left(\frac{x}{l},\frac{y}{l}\right) \text{ , and} \tag{S2}$$

$$a(x,y) = \exp\left(i\frac{2\pi x}{\lambda}\sin\theta\right)\mathrm{comb}\left(\frac{x}{d},\frac{y}{d}\right) \ . \tag{S3}$$

Here, l and d represent the width of the micromirror and the pitch of the micromirror array, respectively. "$*$" denotes two-dimensional (2D) convolution[1]. The case of BiPE superpixels uses $\theta = 0°$ corresponding to the illumination of the PLM at a normal incidence, whereas binary amplitude-based superpixels, assuming the use of a digital micromirror device (DMD), use $\theta = 2\theta_{\mathrm{m}}$ where θ_{m} is the DMD's angle of tilt-actuation, normally ±12°. The scalar field produced at the focal plane of L1 may then be obtained[2] via the Fourier transform of equation (S1),

$$U(f_x,f_y) \propto \mathrm{sinc}(lf_x,lf_y) \times \mathrm{comb}\left(d\left(f_x - \frac{\sin\theta}{\lambda}\right),df_y\right) \ , \tag{S4}$$

where the spatial frequencies f_x and f_y obey the relationships $f_x = \frac{x'}{\lambda f}$ and $f_y = \frac{y'}{\lambda f}$ with respect to L1's focal length f and spatial coordinates x' and y' in the focal plane. The diffraction intensity envelope due to the micromirrors of the SLM may then be given as,

$$I_{\mathrm{env}}(x',y') \propto \mathrm{sinc}^2\left(\frac{lx'}{\lambda f},\frac{ly'}{\lambda f}\right) \ . \tag{S5}$$

The relative diffraction envelope efficiency of BiPE and binary amplitude-based superpixels, assuming the use of SLMs with identical micromirror sizes and array spacings, may be found by evaluating equation (S5) at the locations of the spatial filter positions for each respective method. Using the values $\lambda = 532$ nm, $l = 10.5$ μm, $d = 10.8$ μm, and $f = 150$ mm corresponding to the PLM[3] and the setup in this work, we obtain the increase of diffraction efficiency for BiPE superpixels of 35.0% and 17.2% for $n = 3$ and $n = 4$ respectively, relative to those of binary amplitude-based superpixels.

Supplementary Note 4: Comparison of the gamut space for CFM based on BiPE and binary amplitude-based superpixels

The use of phase modulation rather than amplitude modulation affords considerable benefits in terms of light efficiency and the granularity of the field phasors addressable by superpixel states in BiPE-superpixel-based CFM. To evaluate this benefit, we analyze the gamuts (i.e. sets of all possible field outputs) for both BiPE "PLM" superpixels and binary amplitude-based "DMD" superpixels with a focus on the two cases of practical importance, namely $n = 3$ and $n = 4$.

The state of binary pixels in an SLM superpixel can be specified by using a configuration vector $\boldsymbol{c}$ of n^2 elements with $c_k \in \{0,1\}$ and $k = 0, \cdots, n^2 - 1$ according to row-major ordering. For BiPE superpixels, assuming uniform illumination and assigning the configuration values $c_k = 0$ and $c_k = 1$ to pixel phase shifts of 0 and π radians respectively, the corresponding output field is proportional to

$$U_{\mathrm{PLM}}(\boldsymbol{c}) = \sum_{k=0}^{n^2-1} \exp\left[i\pi\left(\frac{k}{n^2} + c_k\right)\right] \ . \tag{S6}$$

Alternatively, for binary amplitude-based superpixels, assigning the configuration values $c_k = 0$ and $c_k = 1$ to pixels in the "OFF" or "ON" states respectively, the corresponding output field is proportional to

$$U_{\mathrm{DMD}}(\boldsymbol{c}) = \sum_{k=0}^{n^2-1} c_k \exp\left[i\frac{2\pi k}{n^2}\right] \ . \tag{S7}$$

Considered as complex functions across the domain of all 2^{n^2} possible configuration vectors, the gamuts of $U_{\mathrm{PLM}}(\boldsymbol{c})$ and $U_{\mathrm{DMD}}(\boldsymbol{c})$ for the case of $n = 4$ are shown in Fig. S3. As is clear from the figure, two characteristics distinguish these gamuts. First, the maximum complex magnitudes achieved by $U_{\mathrm{PLM}}(\boldsymbol{c})$ and $U_{\mathrm{DMD}}(\boldsymbol{c})$, measured as $R_{\mathrm{PLM}} = 10.20$ and $R_{\mathrm{DMD}} = 5.13$ respectively, differ considerably owing to the additional contributions to constructive interference available to

BiPE superpixels. Second, while direct computation of the gamut produced by $U_{\mathrm{DMD}}(\boldsymbol{c})$ results in a set of 6,561 unique points, computation of the gamut produced by $U_{\mathrm{PLM}}(\boldsymbol{c})$ results in a much enlarged set of 65,536 unique points, representing a completely redundancy-free mapping of configuration vectors to complex field outputs. For other values of n applicable to superpixel-based CFM, an inspection of the gamut sets shows that, while $U_{\mathrm{PLM}}(\boldsymbol{c})$ is not a one-to-one mapping in all cases, the approximately 2-fold increase in the range of field amplitudes accessible by $U_{\mathrm{PLM}}(\boldsymbol{c})$ over $U_{\mathrm{DMD}}(\boldsymbol{c})$ appears to remain true in general.

Finally, we observe that the gamut of any amplitude-based superpixel will include the zero-amplitude phasor (i.e., $0 + 0i$) simply due to the possibility of setting all pixels to the "OFF" amplitude state. By contrast, zero-amplitude output for BiPE superpixels relies on achieving perfectly destructive interference, a situation that while possible in the $n = 3$ case, is not combinatorically possible for all values of n, including $n = 4$. In general, it can be shown that the configuration vector with alternating bits (i.e. $\boldsymbol{c} = (0,1,0,1,\dots,0)$) always produces $U_{\mathrm{PLM}}(\boldsymbol{c}) = 0$ when n is odd. Using this result, it can be further shown that zeros occur in the gamut whenever n possesses an odd factor. Values of n that are powers of 2 however, the only exceptions to these cases, appear to lack configurations satisfying $U_{\mathrm{PLM}}(\boldsymbol{c}) = 0$. Nonetheless, near-zero amplitudes are always possible. For example, the gamut of $n = 4$ BiPE superpixels exhibits a sharp lower bound in the magnitude of $|U_{\mathrm{PLM}}(\boldsymbol{c})| \geq 0.00812\, R_{\mathrm{PLM}}$.

Supplementary Note 5: Details of the PLM display of BiPE superpixels

We here describe the processing and data formatting steps necessary for the display of BiPE superpixel patterns on the PLM. Following the determination of an n^2-bit configuration vector $C(u,v)$ for each superpixel according to equation (2) in the Main Text, we reshape these vectors into $n \times n$ blocks according to row-major ordering followed by a 2D concatenation of all such blocks within the superpixel array. Specifically, writing $c_k(u,v)$ $(k = 0,\dots,n^2-1)$ for the elements of $C(u,v)$, the row-major reshaping operation is defined as

$$\tilde{C}(u,v) = \begin{bmatrix} c_0(u,v) & c_1(u,v) & \dots & c_{n-1}(u,v) \\ c_n(u,v) & c_{n+1}(u,v) & \dots & c_{2n-1}(u,v) \\ \vdots & \vdots & \ddots & \vdots \\ c_{(n-1)n}(u,v) & c_{(n-1)n+1}(u,v) & \dots & c_{n^2-1}(u,v) \end{bmatrix}, \qquad \text{(S8)}$$

with the 2D concatenation of blocks carried out as

$$M = \begin{bmatrix} \tilde{C}(0,0) & \tilde{C}(1,0) & \dots & \tilde{C}(\widetilde{W}-1,0) \\ \tilde{C}(0,1) & \tilde{C}(1,1) & \dots & \tilde{C}(\widetilde{W}-1,1) \\ \vdots & \vdots & \ddots & \vdots \\ \tilde{C}(0,\widetilde{H}-1) & \tilde{C}(1,\widetilde{H}-1) & \dots & \tilde{C}(\widetilde{W}-1,\widetilde{H}-1) \end{bmatrix}, \tag{S9}$$

where $\widetilde{W} = \left\lfloor \frac{W}{n} \right\rfloor$ and $\widetilde{H} = \left\lfloor \frac{H}{n} \right\rfloor$ denote the width and height of the superpixel array. Since typical values of n used in practice are small, situations in which $\frac{W}{n}$ or $\frac{H}{n}$ are not integers may be accommodated by the insertion of a small amount of padding data at the edges of M without significant disturbance to modulated fields.

Although M thus defined completely encodes the desired states of binary phase actuation over the PLM's micromirror array, additional bit-wise binary formatting must be carried out in order for the data of M to correctly configure the micromirrors on the actual PLM (see also Supplementary Note 1 and Fig. S1). The conversions take place as follows. For each micromirror, piston displacement is controlled by four electrodes that are individually addressed through CMOS memory cells arranged as a 2×2 block $\begin{bmatrix} b_0 & b_1 \\ b_2 & b_3 \end{bmatrix}$ where each b_i represents a 1-bit value. Letting $E_0, \dots, E_3 \in \{0,1\}$ denote the energized states of the electrodes arranged in order of increasing displacement influence (i.e. area) with "OFF" and "ON" states represented by 0 and 1 respectively, control of the electrodes takes place according to $\begin{bmatrix} E_1 & E_3 \\ E_0 & E_2 \end{bmatrix} = \begin{bmatrix} \bar{b}_0 & b_1 \\ \bar{b}_2 & b_3 \end{bmatrix} = \begin{bmatrix} 1-b_0 & b_1 \\ 1-b_2 & b_3 \end{bmatrix}$, where the inversion of memory cells b_0 and b_2 is stipulated by the structure of CMOS memory to drive the respective electrodes. The states of zero and maximum displacement, actuated by the de-energizing or energizing all electrodes, are thus achieved via storage of the blocks $\begin{bmatrix} 1 & 0 \\ 1 & 0 \end{bmatrix}$ and $\begin{bmatrix} 0 & 1 \\ 0 & 1 \end{bmatrix}$ respectively into the appropriate locations in memory (see Fig. S1d). According to this scheme, the final required control pattern $\widetilde{M}$ written to the PLM device is obtained by the block-wise substitution of $\begin{bmatrix} 1 & 0 \\ 1 & 0 \end{bmatrix}$ and $\begin{bmatrix} 0 & 1 \\ 0 & 1 \end{bmatrix}$ for the values of 0 and 1 respectively in M, thus resulting in a binary array of size $2W \times 2H$. Mathematically, this operation may be compactly expressed as

$$\widetilde{M} = \frac{1}{2}\left[(2M-1) \otimes \left(2\begin{bmatrix} 0 & 1 \\ 0 & 1 \end{bmatrix} - 1\right) + 1\right], \tag{S10}$$

where the operator $\otimes$ denotes the Kronecker matrix product.

Supplementary Note 6: Details of complex field characterization and background compensation

To measure the complex optical fields created by BiPE superpixels, a coherent reference field combined with fringe analysis was used to extract amplitude and phase data from intensity images recorded by the CCD sensor. Two fringe analysis approaches were used to accommodate the characterization of complex fields from either multi-frame or single-frame datasets. In all cases, background compensation of both amplitude and phase data was carried out from the separate characterization of the reference field under the condition of the PLM displaying a BiPE superpixel pattern corresponding to a uniform field.

Complex field measurement from multi-frame data

For experiments that permitted the measurement of multiple CCD images for the characterization of fields, conventional fringe shifting was used, which was driven by uniform phase offsets encoded into the target fields displayed on the PLM. This procedure took place as follows. $A_1(x,y)$ and $\phi_1(x,y)$ and $A_2(x,y)$ and $\phi_2(x,y)$ are written for the spatial amplitude and phase maps of the reference and PLM-produced fields, respectively. Intensity patterns produced from the interference of the reference field with a sequence of phase-shifted PLM fields are expressed as

$$\begin{aligned} I_k(x,y) &= \left|A_1(x,y)\exp[i\phi_1(x,y)] + A_2(x,y)\exp\left[i\left(\phi_2(x,y)+\frac{2\pi k}{K}\right)\right]\right|^2 \\ &= A_1^2(x,y) + A_2^2(x,y) + 2A_1(x,y)A_2(x,y)\cos\left(\phi_1(x,y)-\phi_2(x,y)-\frac{2\pi k}{K}\right) , \end{aligned} \tag{S11}$$

where the integer K denotes the fixed number of fringe patterns to be collected, and the indices k range over $k = 0, \ldots, K-1$. Extraction of amplitude and phase information from the recorded images $I_k(x,y)$ may then be accomplished with the use of the standard fringe shifting algorithm[4–6] according to

$$A_1(x,y)A_2(x,y) = \frac{1}{K}\left[\left(S_1(x,y)\right)^2 + \left(S_2(x,y)\right)^2\right]^{1/2} \text{..and} \tag{S12}$$

$$\phi_1(x,y) - \phi_2(x,y) = \tan^{-1}\left(S_1(x,y)/S_2(x,y)\right) , \tag{S13}$$

where

$$S_1(x,y) = \sum_{k=0}^{K-1} I_k(x,y)\sin(2\pi k/K) \text{ and} \tag{S14}$$

$$S_2(x,y) = \sum_{k=0}^{K-1} I_k(x,y)\cos(2\pi k/K) . \tag{S15}$$

Using a quadrant-sensitive inverse tangent function for the computation of equation (S13) allows recovered phases to be considered in the interval $[0,2\pi)$. Starting from a target field $\tilde{T}(u,v)$, control of the phase shifting of PLM fields was handled via the specification of modified target fields $\tilde{T}_k(u,v) = \tilde{T}(u,v)\exp(i2\pi k/K)$. Recovery of amplitude and phase from the PLM fields then followed from equations (S12) and (S13), together with reference field data obtained from the same procedure carried out with the flat target fields $\tilde{T}_k(u,v) = \exp(i2\pi k/K)$ corresponding to $A_2(x,y) = 1$ and $\phi_2(x,y) = 0$.

To reduce the influence of drift due to environmental factors between the measurement of PLM and reference field data, the value of $K = 12$ was chosen thus allowing for the collection of both datasets to proceed via the display of a single 24-bit color image whose individual bitplanes were displayed by the PLM at 1.44 kHz (see Supplementary Note 1). Specifically, the PLM control image packaged in the j^{th} sequentially displayed biplane was determined by the sequence of target fields

$$\tilde{T}_j(u,v) = \begin{cases} \tilde{T}(u,v)\exp(i2\pi j/K) & \text{for } j < K \\ \exp(i2\pi(j-K)/K) & \text{for } j \geq K \end{cases}, \tag{S16}$$

for $j = 0, \ldots, 2K-1$.

Complex field measurement from single-frame data

For the characterization of complex fields at high speed, a method based on the Fourier transform[5] was used that allowed for the recovery of amplitude and phase information from only a single interferogram. The principle of this method may be understood as follows. Discarding the contributions of fringe shifting, equation (S11) may be expressed in the form

$$I(x,y) = A_1^2(x,y) + A_2^2(x,y) + A_1(x,y)A_2(x,y)\left(e^{i\Delta} + e^{-i\Delta}\right), \tag{S17}$$

where $\Delta = \phi_1(x,y) - \phi_2(x,y)$. This equation shows that taking the 2D Fourier transformation of $I(x,y)$ allows for the removal of the DC and conjugate terms in equation (S17) via the application of the appropriate filters. The filtered complex-valued image $\tilde{I}(x,y)$ then obtained can be expressed as

$$\tilde{I}(x,y) = A_1(x,y)A_2(x,y)e^{i\Delta}, \tag{S18}$$

from which recovery of amplitude and phase information follows according to

$$A_1(x,y)A_2(x,y) = \left|\tilde{I}(x,y)\right| \text{ and} \tag{S19}$$

$$\phi_1(x,y) - \phi_2(x,y) = \tan^{-1}\left(\frac{\mathrm{Im}\left(\tilde{I}(x,y)\right)}{\mathrm{Re}\left(\tilde{I}(x,y)\right)}\right) , \tag{S20}$$

where $\mathrm{Re}(\cdot)$ and $\mathrm{Im}(\cdot)$ denote the extraction of the real and imaginary components, respectively. Single-frame recovery of amplitude and phase from PLM fields then follows from (S19) and (S20) together with reference field data obtained by the PLM display of the target field $\tilde{T}(u,v) = 1$.

Supplementary Note 7: Details of BiPE-superpixel-based CFM used for augmented reality display

For the demonstration of augmented reality (AR) display using BiPE superpixel-based CFM, it was necessary to determine a mapping relationship between the coordinates of superpixels on the surface of the PLM and the pixel coordinates on the CCD sensor used for image capture. This mapping was modeled as a planar projective transformation[7,8] estimated using four registration point pairs at the corners of the PLM's FOV in the sensor plane of the camera. An estimation of this mapping was achieved as follows. The transformation was modeled as a mapping between coordinate systems $(x,y) \rightarrow (x'',y'')$ represented by a 3×3 matrix transformation operating on homogeneous coordinate representations $[x,y,1]^T$ and $[x'',y'',1]^T$ of the input and output coordinates (x,y) and (x'',y''), respectively. Mathematically, this mapping was defined by

$$s\begin{bmatrix} x'' \\ y'' \\ 1 \end{bmatrix} = \begin{bmatrix} h_1 & h_2 & h_3 \\ h_4 & h_5 & h_6 \\ h_7 & h_8 & h_9 \end{bmatrix}\begin{bmatrix} x \\ y \\ 1 \end{bmatrix} , \tag{S21}$$

where the scalar s constituted a conversion from homogeneous coordinates required for the extraction of x'' and y''. Because of equivalence up to an overall scale factor, the nine elements $h_r \;\; r = 1,\ldots,9$ represent eight degrees of freedom that may be determined exactly by the constraints provided by four pairs of known coordinate mappings $(x_s,y_s) \rightarrow (x_s'',y_s'')\; s = 1,\ldots,4$. Substituting this data into equation (S21) allows the h_r to be determined via a single homogeneous linear equation of rank eight; a procedure known as the direct linear transform (DLT) algorithm for homography estimation[7].

Measurement of the four control point coordinates used by the DLT algorithm was achieved as follows. First, a dedicated calibration image was displayed on the PLM and imaged to the camera with the light path from the scene blocked. The calibration image consisted of four

spots of maximum brightness located at chosen coordinates near the corners of the PLM field. Each spot consisted of a 2×2 group of superpixels configured to output maximum brightness, as well as a directly displayed numeric label included to facilitate correct matching. Analysis of the camera image then allowed for the extraction of the transformed coordinates as the centroid of intensity for each spot.

After the determination of the projective transformation, the creation of PLM images achieving scene-matched AR display took place as follows. First, an image of the real scene was captured by the camera without PLM illumination. This operation allowed for the offline design of 24 animation frames of complimentary scene imagery to take place within the camera pixel coordinate system using digital illustration software. Translation of this imagery to PLM images then took place via the projective transformation followed by bi-linear interpolation resampling and the assignment of superpixel mirror configuration vectors as described in the Main Text. Compensation of image inversion in the optical path took place automatically from the point-pair information used for the estimation of the homography. Animated AR display was then carried out at a rate of 1.44 kHz, with camera capture occurring synchronously via start frame trigger signals provided by the PLM hardware. Finally, additional images consisting of PLM-contributed lighting were also obtained that allowed for the results presented in Main Text Fig. 6 to feature artificial colors for distinguishing the lighting effects due to PLM display. Raw data from this experiment without artificial colors is shown in Fig. S4.

SUPPLEMENTARY REFERENCES

1. Liang, J. et al. Grayscale laser image formation using a programmable binary mask. *Optical Engineering* **51**, 108201 (2012).

2. Goodman, J. W. *Introduction to Fourier Optics*. (New York, W. H. Freeman & Co Ltd, 2017).

3. Bartlett, T. A. et al. Recent advances in the development of the Texas Instruments phase-only microelectromechanical systems (MEMS) spatial light modulator. Proceedings of SPIE 11698, Emerging Digital Micromirror Device Based Systems and Applications XIII. SPIE, 2021, 116980O.

4. Zuo, C. et al. Phase shifting algorithms for fringe projection profilometry: a review. *Optics and Lasers in Engineering* **109**, 23–59 (2018).

5. Zhang, S. High-speed 3D shape measurement with structured light methods: a review. *Optics and Lasers in Engineering* **106**, 119–131 (2018).

6. Kilcullen, P., Jiang, C., Ozaki, T. & Liang, J. Camera-free three-dimensional dual photography. *Optics Express* **28**, 29377–29389 (2020).

7. Richard Hartley & Andrew Zisserman. *Multiple View Geometry in Computer Vision*. (Cambridge University Press, 2004).

8. Jiang, C. et al. High-speed dual-view band-limited illumination profilometry using temporally interlaced acquisition. *Photonics Research* **8**, 1808–1817 (2020).

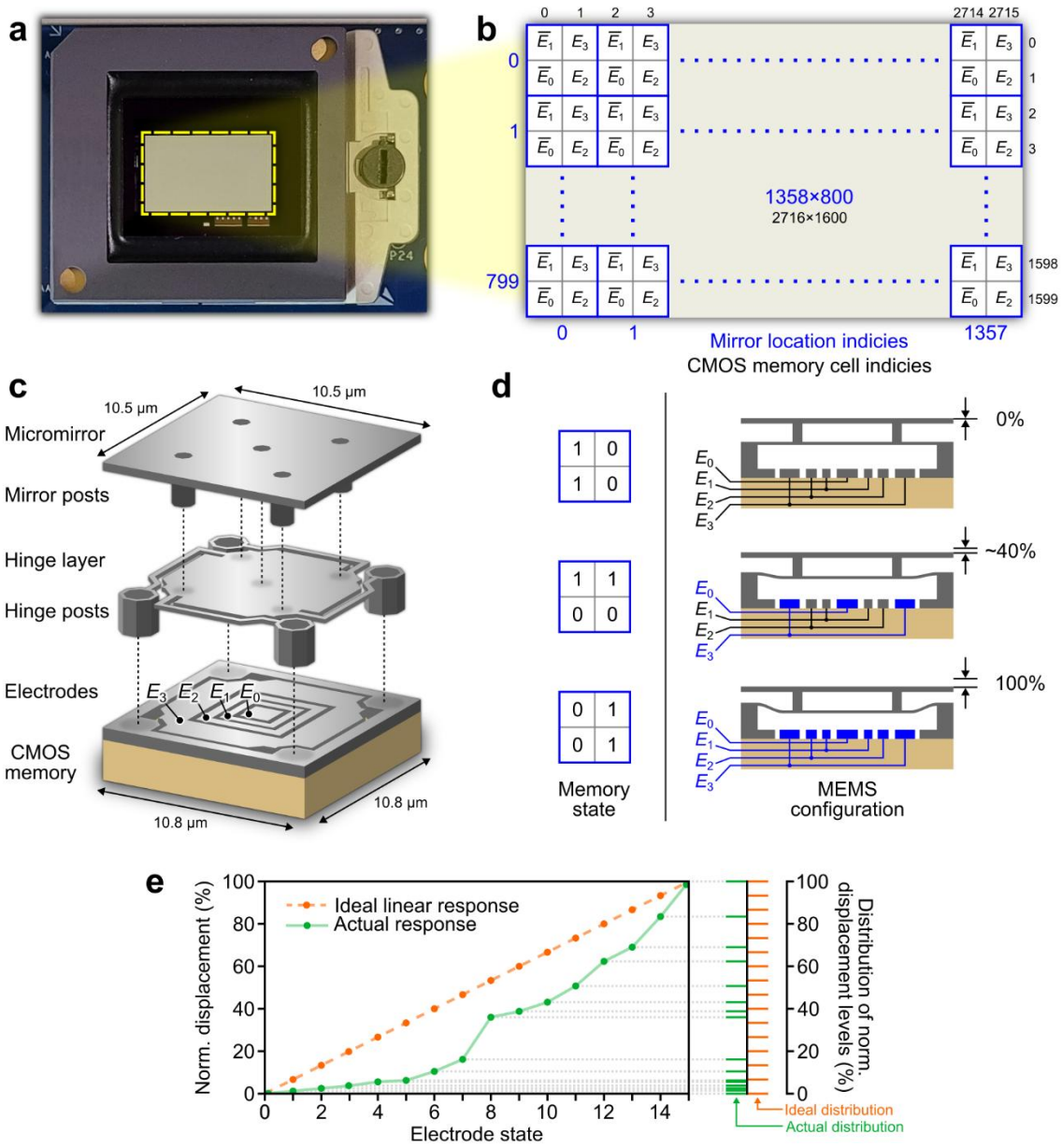

Fig. S1

Structure and operation of the Texas Instruments PLM. a Photograph of the mounted PLM chip. **b** Memory map showing the correspondence between CMOS memory cells and the four actuation electrodes of each mirror. Overbars $\bar{E}_0$ and $\bar{E}_1$ indicate inversion of the stored bits when used to drive the corresponding electrodes. **c** Exploded view of the MEMS structure of each micromirror. **d** Cross-section diagram illustrating the piston-mode actuation of a micromirror through the energizing (highlighted in blue) of selected electrodes by values written to CMOS memory. **e** Normalized micromirror displacement response illustrated as a function of electrode state (left) and as a distribution of displacement levels (right), adapted from data reported in Supplementary Reference [3].

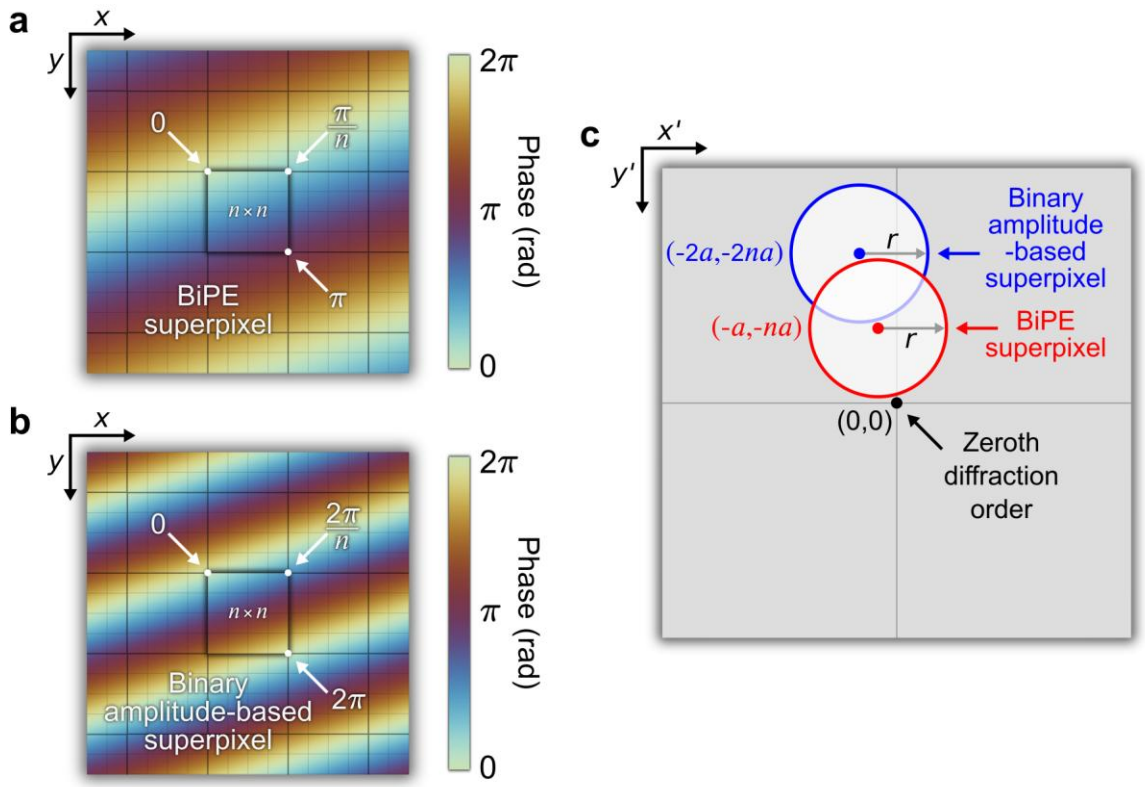

Fig. S2

Comparison of spatial filtering requirements between BiPE and binary amplitude-based superpixels. a Illustration of the SLM phase pre-factor used for BiPE superpixel CFM ($n = 4$), with boundary phase values and the footprint of one superpixel highlighted. **b** As in (**a**), but for CFM using binary amplitude-based superpixels. **c** Spatial filter positions for BiPE and binary amplitude-based superpixels illustrated in units of $a = \frac{\lambda f}{2dn^2}$ at the Fourier plane.

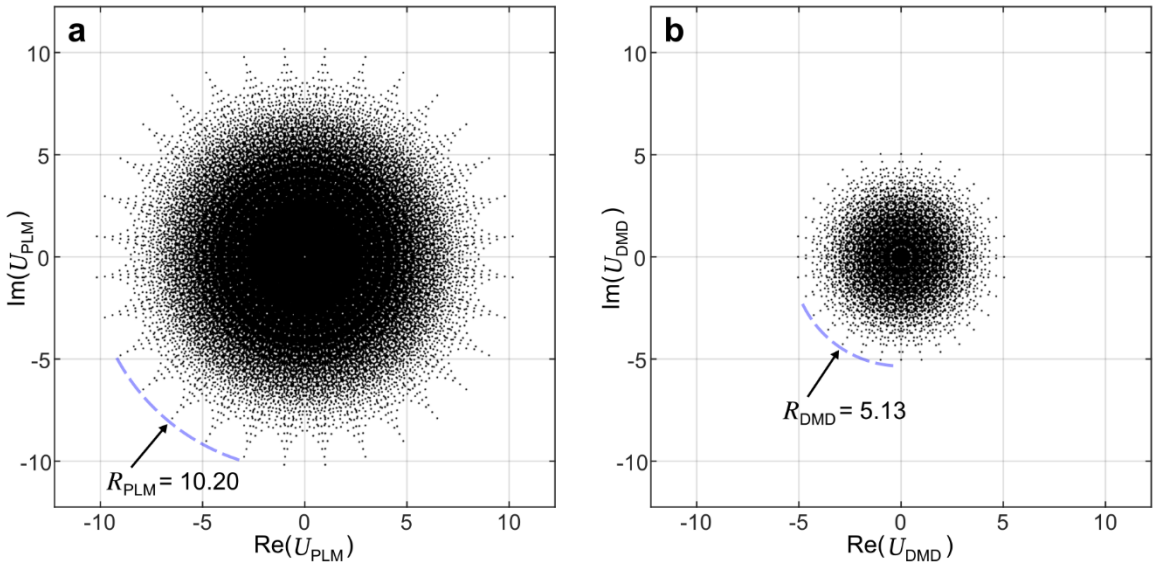

Fig. S3

Comparison of gamut space between BiPE and binary amplitude-based superpixels. a Gamut of complex field values (65,536 unique points) achievable by a 4×4 BiPE superpixel. **b** Gamut of complex field values (6,561 unique points) achievable by a 4×4 binary amplitude-based superpixel.

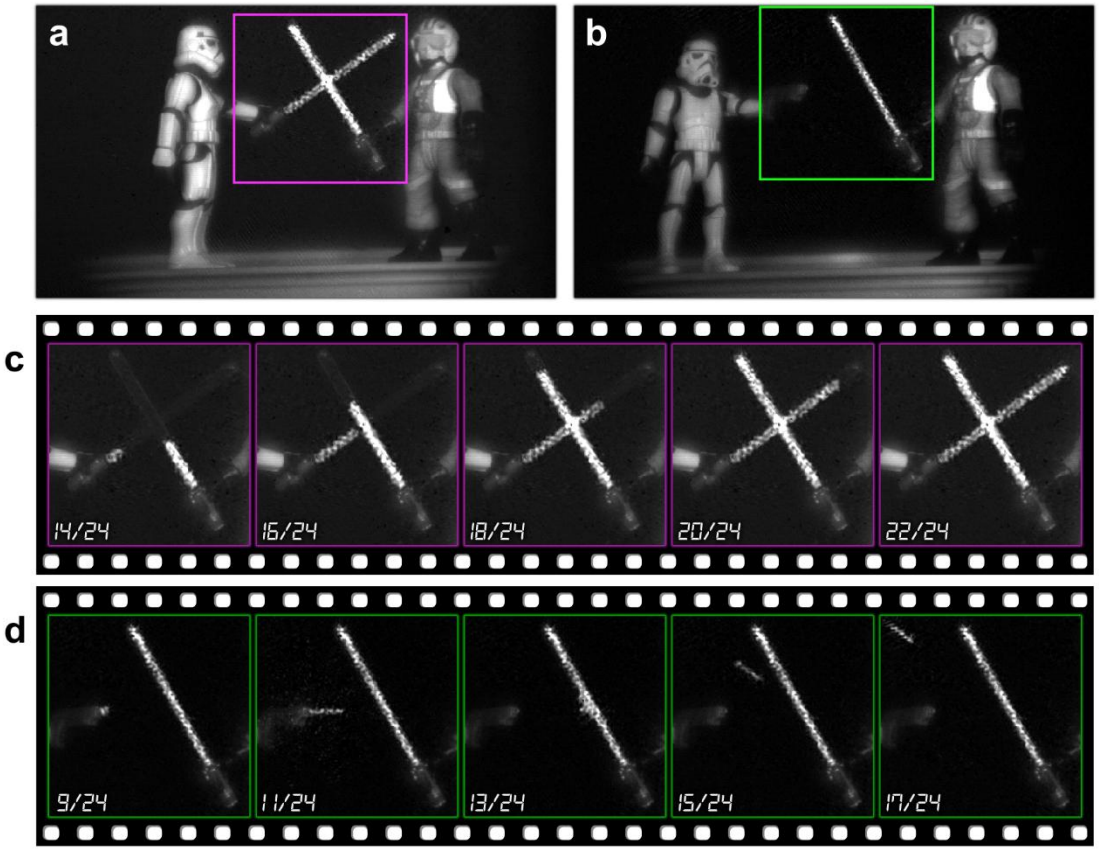

Fig. S4

Raw data for AR display using BiPE-superpixel-based CFM. a,b Scene overviews showing figurine poses and AR displayed by the PLM. **c** Sequence of selected animation frames from the AR scene in (**a**). **d** Sequence of selected animation frames from the AR scene in (**b**).

Supplementary Tables

Method of CFM	Phase gradient (rad·m^{-1})	Spatial filter position (m)
BiPE superpixel	$\left(\frac{\pi}{dn^2}, \frac{\pi}{dn}\right)$	$\left(\frac{-\lambda f}{2dn^2}, \frac{-\lambda f}{2dn}\right)$
Binary amplitude-based superpixel	$\left(\frac{2\pi}{dn^2}, \frac{2\pi}{dn}\right)$	$\left(\frac{-\lambda f}{dn^2}, \frac{-\lambda f}{dn}\right)$

Table S1
Comparison of the phase gradient (x, y) and the spatial filter positions (x', y') for CFM based on BiPE superpixels and binary amplitude-based superpixels.